Low-Temperature Aging Provides 22% Efficient Bromine-Free and Passivation Layer-Free Planar Perovskite Solar Cells

Xin Wang[1], Luyao Wang[1], Tong Shan[2], Shibing Leng[1], Hongliang Zhong[2], Qinye Bao[3], Zheng-Hong Lu[4] ✉, Lin-Long Deng[5] ✉, Chun-Chao Chen[1] ✉

✉ Zheng-Hong Lu, zhenghong.lu@utoronto.ca; Lin-Long Deng, denglinlong@xmu.edu.cn; Chun-Chao Chen, c3chen@sjtu.edu.cn

[1] School of Material Science and Engineering, Shanghai Jiao Tong University, Shanghai 200240, People's Republic of China

[2] School of Chemistry and Chemical Engineering, Shanghai Jiao Tong University, Shanghai 200240, People's Republic of China

[3] Key Laboratory of Solar Materials and Devices, Department of Electronic Science, School of Physics and Electronic Science, East China Normal University, Shanghai 200240, People's Republic of China

[4] Department of Materials Science and Engineering, University of Toronto, 184 College Street, Toronto, ON M5S 3E4, Canada

[5] Pen-Tung Sah Institute of Micro-Nano Science and Technology, Xiamen University, Xiamen 361005, People's Republic of China

ARTICLE HIGHLIGHTS

- By low-temperature aging, superior bromine-free $FA_{1-x}MA_xPbI_3$ perovskite film is realized.

- By suppressing lead iodide on the surface of perovskite, no further passivation step or layer is needed. The efficiency of planar perovskite solar cells is improved to 22.41% with robust reproducibility.

ABSTRACT Previous reports of formamidinium/methylamine (FAMA)-mixed halide perovskite solar cells have focused mainly on controlling the morphology of the perovskite film and its interface—for example, through the inclusion of bromine and surface passivation. In this paper, we describe a new processing pathway for the growth of a high-quality bromine-free $FAMAPbI_3$ halide perovskites via the control of intermediate phase. Through low-temperature aging growth (LTAG) of a freshly deposited perovskite film, α-phase perovskites can be seeded in the intermediate phase and, at the same time, prevent beta-phase perovskite to nucleate. After postannealing, large grain-size perovskites with significantly reduced PbI_2 presence on the surface can be obtained, thereby eliminating the need of additional surface passivation step. Our pristine LTAG-treated solar cells could provide PCEs of greater than 22% without elaborate use of bromine or an additional passivation layer. More importantly, when using this LTAG process, the growth of the pure alpha-phase $FAMAPbI_3$ was highly reproducible.

KEYWORDS Aging growth; Bromine-free; Passivation layer; Lead iodide; Perovskite solar cells
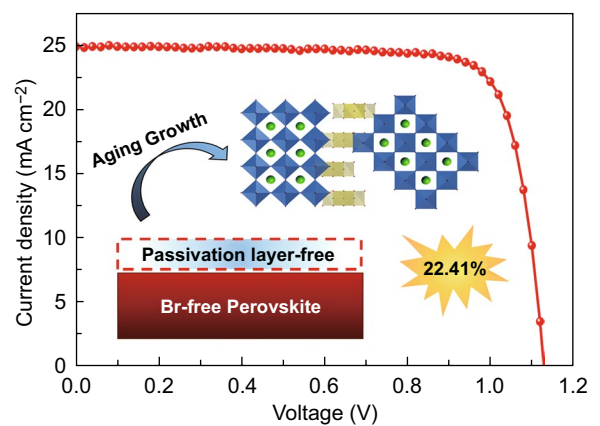
1 Introduction

Organic/inorganic hybrid perovskite solar cells (PSCs) are emerging next-generation photovoltaic technologies that have attracted attention for their dramatic improvements in efficiency—from 3.8% [1] to over 24%—in less than a decade [2], their low manufacturing costs, and their ease of solution processing. To promote the device performance of PSCs beyond 20%, several techniques have been investigated, including variations in composition [3–5], control over the perovskite film growth [6–9], interface engineering [10–12], the use of additives [13–15], ionic liquid technique [16], and surface passivation [17–19]. Among the perovskite materials currently being investigated, the low-band-gap α-phase form-amidinium lead iodide (FAPbI$_3$) perovskite, which possesses an ideal band gap of 1.48 eV and extended light absorption to 840 nm [20–22], appears to have the most promising perovskite composition to achieve record-breaking photocurrent densities and power conversion efficiencies (PCEs) [23–27]. Nevertheless, obtaining the α-phase FAPbI$_3$ in its pure composition is difficult through either one-step anti-solvent deposition or the two-step sequential method [15, 28–30]. Therefore, mixed cation and inclusion of bromine have been employed to stabilize the α-phase FAPbI$_3$ and, thereby, obtain device performances exceeding 21% [31–33]. Unfortunately, the inclusion of bromine also results in unwanted changes in the composition of the perovskite and contributes to a narrower absorption spectrum. Thus, many attempts have been made toward achieving bromine-free, pure α-phase FAPbI$_3$-based solar cells without compromising the intrinsic properties of the FAPbI$_3$ perovskite [34–37].

Two-step sequential deposition methods are the most effective methods for preparing FA-based halide perovskite films in planar n–i–p structures [8, 27, 34]. Previous studies have demonstrated that high-quality perovskite films can be obtained in the presence of moderate amounts of humidity [5, 38]. Interestingly, excess lead iodide (PbI$_2$) also forms during the growth of perovskite films, which originates from the precursor ingredient and decomposes when high-temperature postannealing of the perovskite film is performed in air [39–41]. Some studies have found that the PbI$_2$ by-product has a beneficial effect by passivating the grain boundary defects inside the perovskite film under certain conditions, thereby enhancing device efficiency [32, 40–42]. For example, a small amount of PbI$_2$ can passivate the defects on the interface between the perovskite layer (PVK) and the hole-transporting layer (HTL), thus improving device efficiency and eliminating the hysteresis effect [31, 33, 43]. Nevertheless, excess PbI$_2$ has negative effects. For instance, if too much PbI$_2$ separates out from the perovskite film surface, the thick PbI$_2$ layer may itself function as an insulating layer with increased defect density, rather than acting as a passivation layer [44–46]. Therefore, devices prepared with an excess of PbI$_2$ often have lower open-circuit voltages (V_{oc}) and undergo faster photodegradation, compared to PbI$_2$-deficient devices [44–48]. Therefore, it is necessary to optimize the amount of PbI$_2$ at the PVK–HTL interface to passivate the interface defect states and, thereby, facilitate charge transport.

In several recent studies, efforts have been devoted toward optimizing the passivation layer on the top surface of the perovskite film to remove the excess PbI$_2$, by using various passivators, including organic halide salts. For example, Zhu et al. achieved a high value of V_{oc} of 1.21 V when using guanidinium bromide salts on a control perovskite film; here, the excess PbI$_2$/PbBr$_2$ crystals were "digested" with the assistance of the guanidinium bromide [48]. You et al. recovered the contact energy loss and obtained a certified quasi-steady-state efficiency of 23.32% after passivating excess PbI$_2$ crystals on perovskite film surface with the organic cationic salt of PEAI [34]. Furthermore, negative effects on the underlying perovskite layer have also been found when an inappropriate solvent or layer thickness was used for the passivation layer [17]. To date, the working mechanism of the passivation layer remains unclear. Determining when to use a passivator, or which passivator to use in a given system, with the hope of reducing the effect of excess PbI$_2$ and mitigating non-radiative recombination, can still be a challenge. Developing a passivation layer-free method is important for the fabrication of perovskite layer to be flexible in terms of controlling the ideal amount of PbI$_2$ for the self-passivation of surface defects, while also ensuring that the process is simple and reproducible.

In this paper, we proposed a new method, involving low-temperature aging growth (LTAG) prior to thermal annealing, for the production of high-quality bromine-free perovskite films, with control over the composition of PbI$_2$, from FA$_{1-x}$MA$_x$PbI$_3$ (FA: HC(NH$_2$)$_2$, MA: CH$_3$NH$_3$, hereafter denoted "FAMAPbI$_3$") perovskites for planar n–i–p-type solar cells. We demonstrate that an optimized residual content of PbI$_2$ on the FAMAPbI$_3$ perovskite film surface can

be obtained after aging the as-formed perovskite film at low temperature under N_2 (in a glove box) and annealing in air at a certain relative humidity (RH, 30–40%). Unlike conventional processes that utilize bromine and often lead to a large amount of excess PbI_2 on the top surface, the perovskite films produced using this LTAG method feature with a fine amount of PbI_2 crystals between the grain boundaries and much lower PbI_2 contents on the top surface. Analyses using time-resolved photoluminescence (TRPL) spectroscopy, the space charge-limited current (SCLC) method, ultraviolet photoelectron spectrometry (UPS), and atomic force microscopy (AFM) revealed excellent charge transport and suppressed non-radiative losses at the PVK–HTL interfaces of our LTAG-treated samples. As a result, our champion LTAG devices achieved a record-high PCE-22.41% for a bromine-free $FAMAPbI_3$ perovskite. Without the need for additional processing steps to modify the problematic PbI_2 layer, our present LTAG method can produce suitable amounts of PbI_2 on the top surface of the perovskite layer to provide stable PSC devices exhibiting high efficiency and excellent reproducibility.

2 Experimental Section

2.1 Materials

The SnO_2 colloid precursor (tin oxide, 15% in H_2O colloidal dispersion) was purchased from Alfa Aesar. PbI_2 (99.8%) was purchased from Kanto Chemical. Dimethyl sulfoxide (DMSO 99.8%), chlorobenzene (99.8%), N,N-dimethylformamide (DMF, 99.8%), and isopropanol (IPA, 99.8%) were obtained from Sigma-Aldrich. Lithium bis(trifluoromethylsulfonyl) imide (Li-TFSI, 95%), 4-*tert*-butylpyridine (TBP, 96%), and 2,2′,7,7′-tetrakis-(N,N-di-*p*-methoxyphenylamine)-9,9′-spirobifluorene (Spiro-OMeTAD, 99%) were purchased from Lumtec. Formamidinium iodide $[CH(NH_2)_2I]$ and methylammonium iodide (CH_3NH_3I) were obtained from Dysel. Methylammonium chloride (MACl) was purchased from Xi'an Polymer Light Technology. All chemicals and reagents were used without further purification.

2.2 Solar Cell Fabrication

Patterned ITO glass was cleaned sequentially through sonication in detergent, deionized water, acetone, and isopropyl alcohol. Prior to deposition, the ITO was treated with UV ozone for 15 min. The thin SnO_2 film was formed by spin-coating onto the substrates from a diluted SnO_2 precursor solution (2.67%, in water) at 3500 rpm for 30 s; the sample was then annealed in air at 150 °C for 40 min. After cooling to room temperature, the ITO/SnO_2 substrate was cleaned with UV ozone for 15 min to improve the surface wetting in the following steps. To prepare the perovskite film, 1.5 M PbI_2 in DMF/DMSO (9:1) was spin-coated on the ITO/SnO_2 substrate at 1500 rpm for 30 s, and then the sample was annealed at 70 °C for 1 min. A solution of FAI, MAI, and MACl (90:6:9 mg) in IPA (1 mL) was added dropwise onto the PbI_2 film at 2000 rpm for 30 s; the as-formed fresh film was then converted to a black $FAMAPbI_3$ film through annealing on a hot plate in air at 150 °C for 15 min (30–40% humidity). For low-temperature aging growth (LTAG) of the crystallization process, a fresh film was aged in a glove box at various temperatures for 5 min; the as-formed film was transferred into ambient air for further thermal annealing. After the $FAMAPbI_3$ perovskite film had formed, the sample was transferred to a glove box and then a solution of Spiro-OMeTAD in chlorobenzene (72.3 mg mL^{-1}) containing Li-TFSI solution (17.5 μL; prepared as a 520 mg mL^{-1} solution in MeCN) and TBP (28.8 μL) was spin-coated on the perovskite film at 3000 rpm for 30 s. Finally, a Au film (80 nm) was deposited, as the counter electrode, through thermal evaporation on top of the Spiro-OMeTAD layer. The device size was 0.18 cm^2; the accurate active cell area was 0.1 cm^2, using a non-reflective mask, when measuring.

2.3 Characterization

X-ray diffraction (XRD) patterns were obtained using a Rigaku Ultima IV diffractometer and Cu Ka radiation. Scanning electron microscopy (SEM) images were obtained using a JEOL JSM-7800F Prime scanning electron microscope. UV–Vis absorption spectra were recorded using a Lambda 35 UV–Vis spectrometer. Steady-state fluorescence and time-resolved photoluminescence (TRPL) spectra were recorded using a FLS1000 photoluminescence spectrometer with excitation at a wavelength of 450 nm. Current density–voltage (J–V) curves of the photovoltaic devices were measured using a Keithley 2400 source meter. Photocurrents were measured under AM1.5G illumination at 100 mW cm^{-2} using an Abet Technologies Sun 2000 solar simulator.

External quantum efficiency (EQE) spectra were recorded using an Enlitech LQE-50-FL IPCE measurement system. The light intensity was calibrated using a silicon standard. The active area of each cell was 0.1 cm^2. The *J–V* measurements were recorded in ambient air without encapsulation; both reverse (1.2 → − 0.1 V) and forward (− 0.1 → 1.2 V) scans were performed using the same step of 0.02 V s^{-1}. Electrochemical impedance spectroscopy (EIS) was performed using a Donghua DH7000 electrochemical workstation. Ultraviolet photoelectron spectroscopy (UPS) was performed using an AXIS Ultra DLD instrument with the emitting UV energy at 21.21 eV.

3 Results and Discussion

### 3.1 Fabrication and Characterization of the Perovskite Films

In the low-band-gap FAMAPbI$_3$ perovskite systems, a robust preparation method without bromine is highly desirable to provide devices with higher photocurrent. A new two-step sequential method is presented here to deposit a bromine-free FAMAPbI$_3$ perovskite absorber film. As displayed in Fig. 1a, in the conventional two-step method, PbI$_2$ is dissolved in a mixed solvent of DMF and DMSO. The first step involves formation of a PbI$_2$–DMSO film. In the second step, a solution of the mixed organic FAI and MAI is applied, such that critical intramolecular exchange occurs with the PbI$_2$–DMSO film to form an intermediate-phase FAI–MAI-PbI$_2$–DMSO film [26]. Typically, the brown fresh film is directly subjected to high-temperature annealing in air at a controlled humidity (RH, 30–40%) to allow the highly crystallized perovskite films to form [6]. However, the freshly prepared intermediate film usually transforms, within approximately 10 s, into a yellow δ-phase FAMAPbI$_3$ when exposed to air, resulting in a white or opaque surface for final perovskite film (Fig. S1). As reported previously [49], the intermediate phase is a layered-structure film that lacks an exact composition. If it is not handled properly, this intermediate phase is highly unstable which can cause problems in the following perovskite crystallization process.

In our LTAG method, as displayed in Fig. 1a, the freshly coated intermediate-phase brown film is first left on a hot plate and aged at various low temperatures for 5 min. Specifically, the low-temperature aging is set at 30, 50, and 70 °C for LTAG-30, LTAG-50, and LTAG-70, respectively. Then, the as-formed aged film is then baked on a hot plate at 150 °C for 15 min to produce the α-phase perovskite film (Fig. S2). To study the mechanism of LTAG process, we performed XRD patterns of the as-formed intermediate-phase films for control and LTAG method (at 30, 50, and 70 °C) after the exposure to air but prior to final high-temperature annealing, as shown in Fig. 1b. For the control film without LTAG treatment, the intermediate phase peaked at 9.3° is clearly observed [29, 50]. The undesired δ-phase perovskite peaked at 11.6° is, however, dramatically high, indicating the existence of δ-phase perovskite inside intermediate film. In LTAG-based film, as displayed in Fig. 1b, no signal of δ-phase FAMAPbI$_3$ is found at 11.6°. The signals at 9.3° and 13° for LTAG-30 indicate that the intermediate phase is well kept for the aging temperature at 30 °C. More importantly, α-phase FAMAPbI$_3$ peaked at 13.94° starts to appear in the intermediate phase after LTAG treatment, indicating LTAG can precrystallize α-phase perovskite [51–53]. With increases of aging temperature to 50 and 70 °C, the PbI$_2$ peak at 12.7° starts to exist. This shows that the intermediate phase is volatile and can easily turn into yellow δ-perovskite phase in the control film, but with the help of LTAG the intermediate film is more likely to nucleate α-phase perovskite.

To further certify this phenomenon, Fourier transform infrared spectroscopy (FTIR) was performed and results are shown in Fig. 1c. The characteristic peak in 1016 cm^{-1} represents S = O stretch, indicating the intermediate FAI–MAI-PbI$_2$–DMSO phase from the coordination between DMSO and MA$^+$, FA$^+$, and Pb^{2+} ions [29, 50]. For control film, the intermediate FAI-MAI-PbI$_2$-DMSO phase exists, and the intensity of intermediate phase decreases when the aging temperature increases and disappears at the temperature of 70 °C. These results indicate that LTAG process can avoid the formation of yellow δ-phase FAMAPbI$_3$ as compared to control process. The conversion of the intermediate-phase film to α-phase perovskite is more thorough by releasing the residual complex compositions (e.g., IPA, MAI, or MACl) in the intermediate film beforehand. In other words, LTAG process can help the intermediate phase to start nucleating α-phase perovskite at low aging temperature and finish the conversion to α-phase perovskite during high-temperature postannealing.

Figure 1d presents XRD patterns of the postannealed perovskite films prepared using various aging temperatures. All
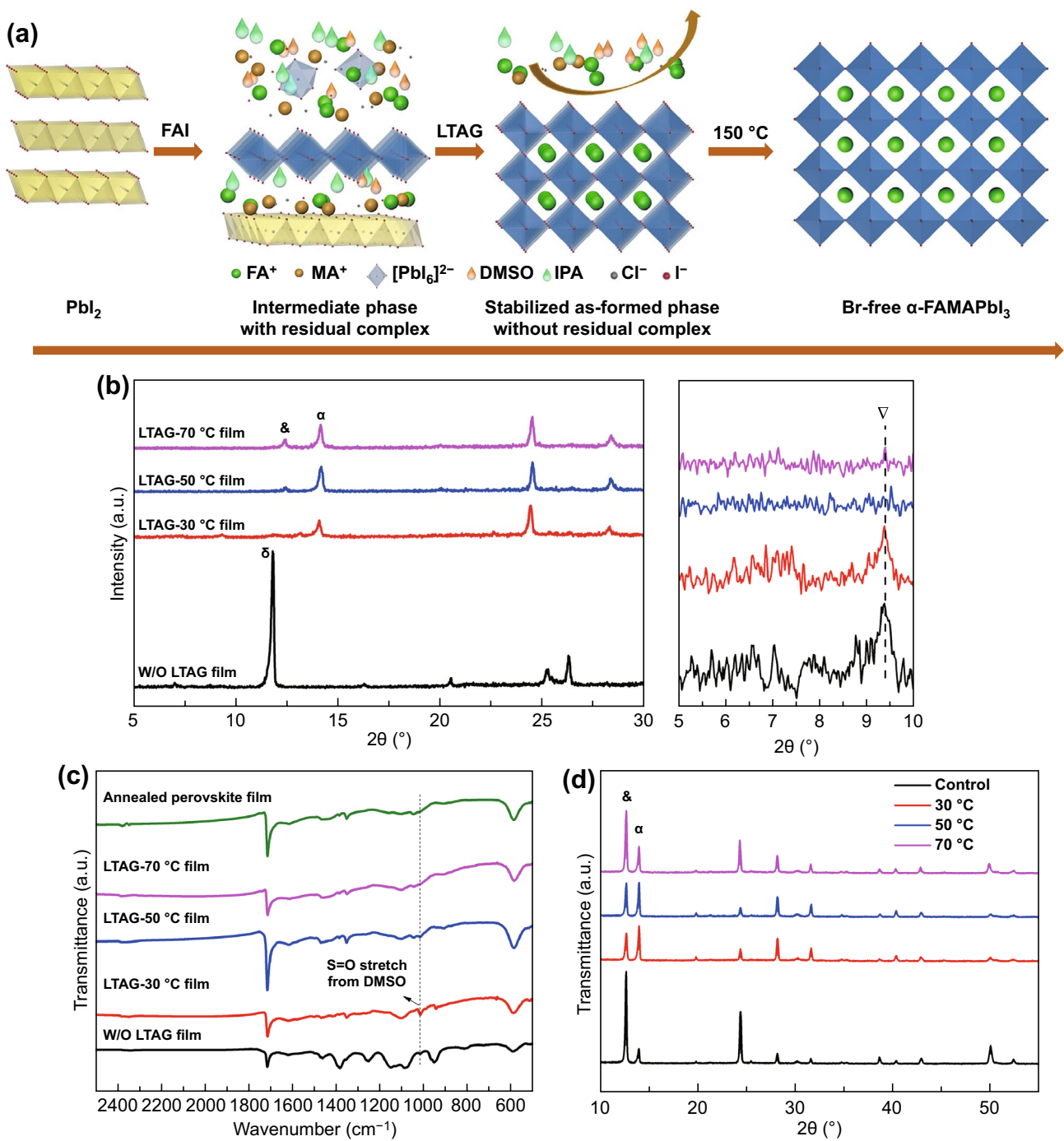
Fig. 1 **a** Schematic representation of the film crystallization process of an LTAG-based FAMAPbI$_3$ perovskite layer. **b** XRD patterns of the as-formed films obtained using the control process and the LTAG method. &, α, δ, ∇ Mean characteristic diffraction signals of the PbI$_2$, black perovskite, yellow perovskite phases, and intermediate phase, respectively. **c** FTIR spectrum of the as-formed film powers using the control process and the LTAG method and for postannealed FAMAPbI$_3$ film. **d** XRD patterns of annealed perovskite layers prepared without (control) and with LTAG treatment (at 30, 50, and 70 °C)

of the samples exhibited characteristic peaks at 12.7° and 13.94°, which were assigned to PbI$_2$ and α-phase perovskite,

corresponding to their (001) and (100) reflections, respectively (Fig. S3) [7]. The intensity of the PbI$_2$ diffraction peak

was remarkably high in the XRD pattern of the control sample. In this case, the PbI_2 diffraction peak was even stronger than that of the perovskite peak. For the LTAG samples, the intensity ratios of the PbI_2 (001) and perovskite (100) signals were much lower than that for the control sample. For low-temperature aging at 30 °C, the intensity of the PbI_2 peak was the lowest among all of our tested samples. The intensity of the PbI_2 peak got stronger with increasing temperature of LTAG method, which was also in consistence with the previous results from XRD and FTIR in the as-prepared films. In other words, the existence of δ-phase in the as-prepared intermediate phase from control process may cause an incomplete conversion of δ-phase to α-phase perovskites, thereby inducing mass nucleation of PbI_2 in the meantime. When using the LTAG method, the α-phase perovskites already precrystallized in the as-prepared intermediate films can help form highly crystallized α-phase perovskite in postannealing step and, at the same time, reduce the presence of PbI_2, which is critically important for the later preparation of high-performance devices [54].

To examine the amount of excess PbI_2, we recorded SEM images of the top surfaces of thermally postannealed perovskite films—one prepared without aging, hereafter denoted as the control sample/film, and three prepared using the LTAG method with aging at temperatures of 30, 50, and 70 °C, hereafter denoted as LTAG-30, LTAG-50, and LTAG-70 samples/films, respectively. In Fig. 2a, for the sample prepared without intermediate film aging, large amounts of bright crystals were present on the surface. In these bright crystals, the dense white areas were formed by PbI_2, while the dark areas were the surrounding perovskite grains [6, 31]. For the LTAG-based perovskite films (Fig. 2b–d), the numbers of white PbI_2 crystals decreased dramatically. The remaining PbI_2 was distributed around the perovskite grain, suggesting a suppressed PbI_2 formation when using the LTAG method. The LTAG-30 sample featured the minimum amount of PbI_2 on the top surface; here, the grain size of the perovskite had increased to 1.15 μm (Fig. S4). The average grain-size distribution obtained from SEM images is exhibited in Fig. S5, indicating that LTAG treatment can restrain the PbI_2 contents and induce a larger grain size of perovskite crystals as compared to that of control samples. These results are also in consistence with the cross-sectional SEM images for control and LTAG-30-treated devices in Fig. 2e, f, an excess amount of PbI_2 is evident on the top surface in control sample, but no PbI_2 is visible on the top

surface for LTAG-30 device. In other words, during the thermal postannealing recrystallization process, the formation of the perovskite crystals and the PbI_2 crystals occurred simultaneously. The LTAG method appeared to seed α-phase perovskites in the intermediate phase and allow the α-phase perovskite crystal grains to grow into larger sizes, thereby limiting the formation of PbI_2 at the surface. In addition, the red shift of absorption edges of LTAG-based perovskite films was observed (Fig. S6). The visible band gap of the LTAG-based films was slightly shifted to a narrower band gap (ca. 1.53 eV). Similar shift has also been found when the content of PbI_2 was decreased on perovskite layer [33].

3.2 Device Fabrication and Characterization

We investigated the efficiencies of solar cells incorporating the perovskite films prepared under the various conditions. The control device and the LTAG-based devices, prepared using aging temperatures of 30, 50, and 70 °C, were fabricated with the following planar configuration: indium tin oxide (ITO)/SnO_2/$FAMAPbI_3$/Spiro-OMeTAD/Au. The thicknesses of the SnO_2, $FAMAPbI_3$ perovskite, and Spiro-OMeTAD layers, determined from cross-sectional SEM images, were 35, 800, and 150 nm, respectively (Fig. S7). Figure 3a presents the current density–voltage (J–V) curves plotted with respect to the aging temperature.

Table 1 summarizes the average photovoltaic parameters obtained from 32 devices subjected to the aging treatment. When the aging temperature was set at 30 °C for LTAG-30, the average PCE of perovskite devices reaches the best performance of 21.4%. Further increase in aging temperature to 50 and 70 °C did not continue to increase the performance but did not keep efficiency at 20%, which is still greatly enhanced from that of the control devices at 18.9% efficiency. Furthermore, 30 °C is the optimal LTAG temperature attributing to its capability to keep the intermediate phase without drying it completely. The proof of this suggestion can be found in Fig. 1b. The control devices provided a low PCE of 19.75%, an open-circuit voltage (V_{oc}) of 1.06 V, a short-current current density (J_{sc}) of 23.96 mA cm^{-2}, and a fill factor (FF) of 0.77. The LTAG-based devices displayed significantly improved photovoltaic performance, particularly in terms of their values of V_{oc} and J_{sc}. For example, the value of J_{sc} of the LTAG-30 sample could exceed 24.40 mA cm^{-2}—the highest measured in this study. The
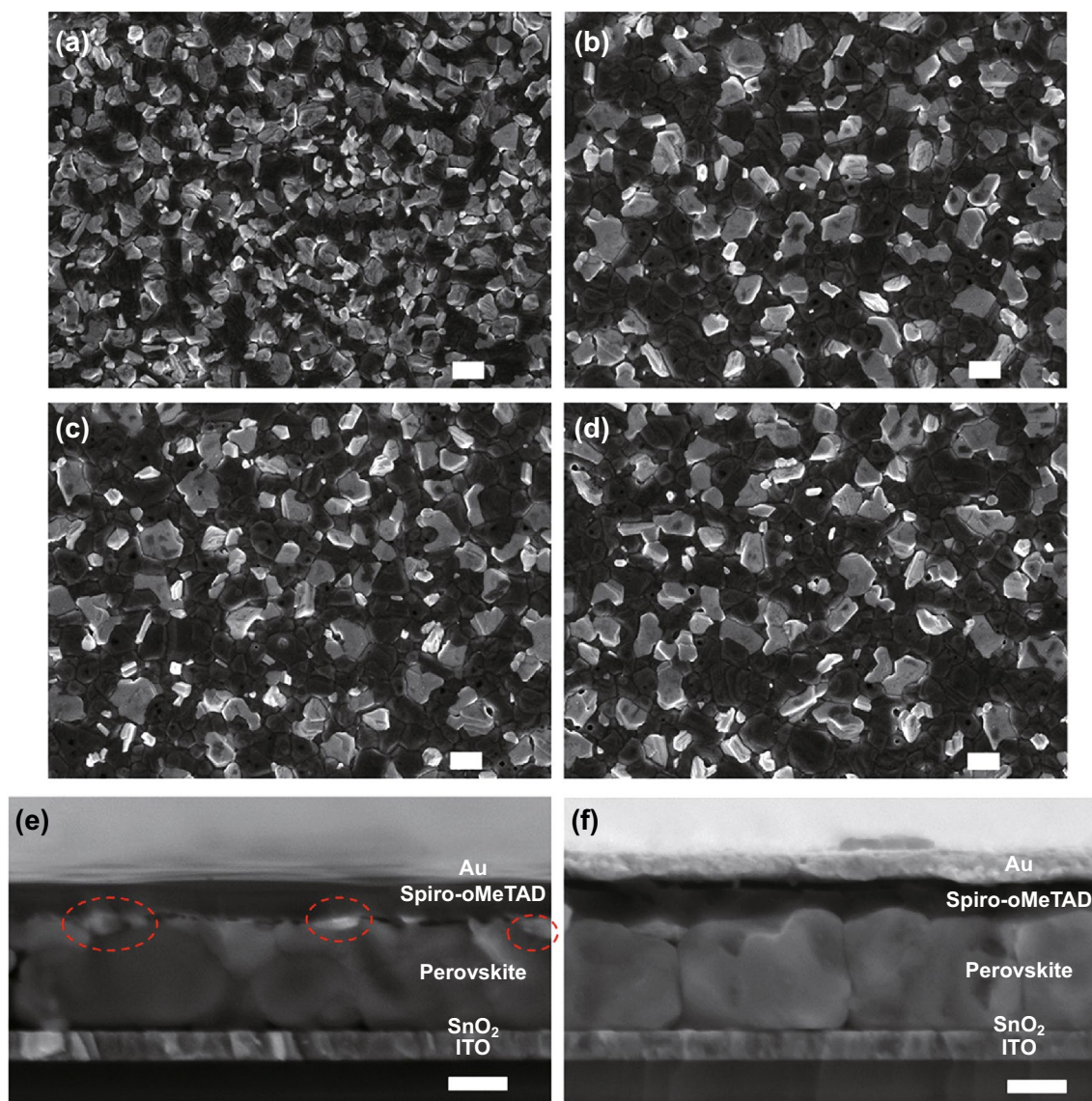
Fig. 2 Top-view SEM images of postdeposition annealed perovskite films: **a** control sample without aging, **b** LTAG-30-treated sample, **c** LTAG-50-treated sample, and **d** LTAG-70-treated sample. Cross-sectional SEM images of **e** control and **f** LTAG-30-treated device; the scale bars: 1 μm (**a–d**); 500 nm (**e, f**)

values of V_{oc} obtained from the devices incorporating the LTAG-treated films that had been aged at 30, 50, and 70 °C were 1.10, 1.12, and 1.10 V, respectively.

Furthermore, we studied the time effect of LTAG (Figs. S8, S9, and Table S1). It was found that 5-min aging time is required to complete LTAG and obtain reduced PbI_2 crystals. When aging time is prolonged over 5 min, there exhibited no significant difference on the morphology and corresponding device performance. These results suggest that decreasing and precisely controlling the PbI_2 content

significantly affected the device performance. Considering that a fine amount of PbI_2 could act as a passivation agent for the grain boundary defects but not affect charge transport at the PVK–HTL contact, we could use the LTAG-30 device, which exhibited the highest performance, to define the optimal content of residual PbI_2 in this study. Indeed, the LTAG-30 device exhibited the highest PCE of 22.41%, with a V_{oc} of 1.12 V, a J_{sc} of 24.79 mA cm^{-2}, and an FF of 0.807 (Fig. 3d). Compared with the results reported previously for FAPbI$_3$-based solar cells prepared without passivation
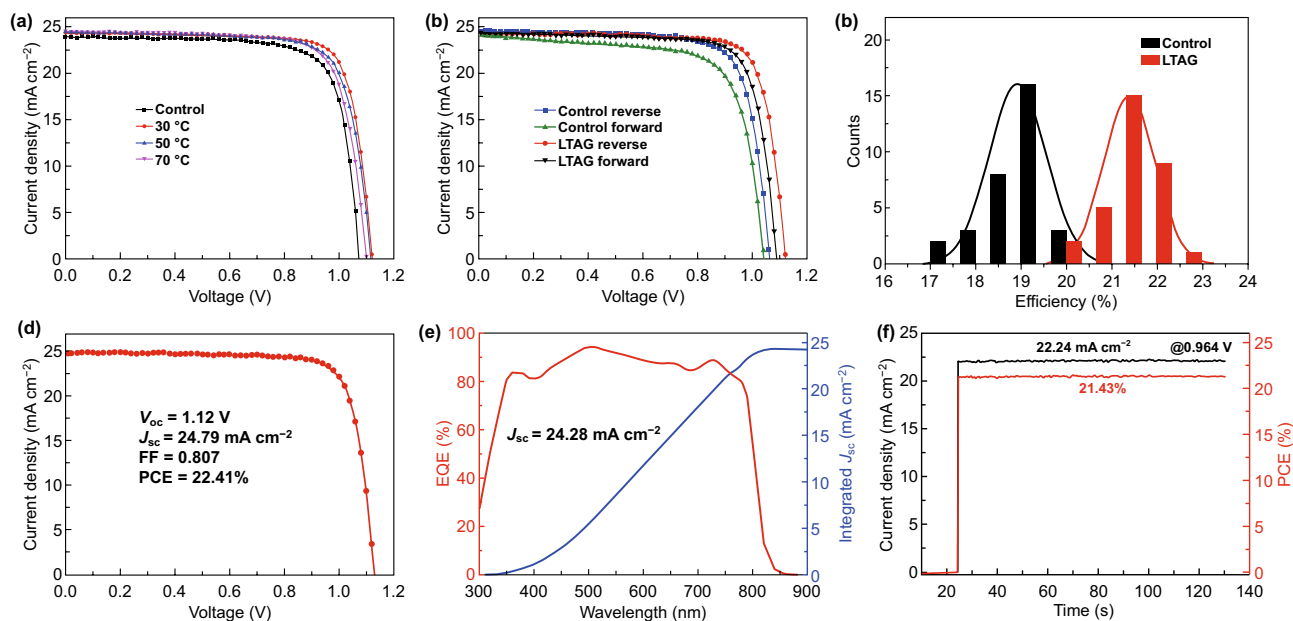
Fig. 3 **a** *J–V* curves of devices prepared using the LTAG method (at 30, 50, and 70 °C), compared with that of the control device. **b** *J–V* curves recorded from reverse and forward scans for the control device and the LTAG-30 solar cell. **c** Distributions of PCEs measured from the control and LTAG-30 devices. **d** *J–V* curve of the best-performing LTAG-30 perovskite solar cell. **e** EQE spectrum and integrated value of J_{sc} of the best-performing LTAG-30 device. **f** Stabilized current density and power output of the best-performing LTAG-30 device, measured close to the maximum power point

Table 1 Average and champion device performance parameters for solar cells processed using the controlled process (control) and the LTAG process (30, 50, 70)

Aging temperature (°C)	V_{oc} (V)	J_{sc} (mA cm^{-2})	FF	PCE (%)	Champion PCE (%)
Control	1.06 ± 0.02	23.5 ± 0.4	0.75 ± 0.03	18.9 ± 0.6	19.75
30	1.12 ± 0.01	24.4 ± 0.4	0.79 ± 0.01	21.4 ± 0.5	22.41
50	1.10 ± 0.02	24.2 ± 0.2	0.76 ± 0.02	20.2 ± 0.7	20.91
70	1.10 ± 0.02	24.1 ± 0.4	0.75 ± 0.02	19.9 ± 0.7	20.67

Thirty-two devices were fabricated for each condition

layers (Table S2), this device efficiency is the highest ever recorded for a bromine- and passivation layer-free planar-structure perovskite solar cells. Furthermore, we tested the device performance when LTAG-based film was annealed in the ambient under different humidity conditions and found that the corresponding device performance exhibited almost no decrease, indicating a better stability toward humidity as compared to the control devices which are found with a significant degradation under high humidity environment (Fig. S10).

We also tested the devices obtained after performing the aging growth under various atmospheres (N_2, Ar, and O_2);

Figure S11 and Table S3 present the corresponding photovoltaic parameters, which reveal that the aging growth treatment was the key factor, rather than the N_2 atmosphere, promoting the greater device performance [55]. We attribute the enhancement in device performance to the lower residual PbI_2, the enhanced light absorption, and the improved charge recombination, as inferred from the XRD, absorption spectral, and PL intensity data.

To examine the hysteresis effects, we measured the J–V curves of the LTAG-based and control devices in reverse and forward scans. As shown in Fig. 3b, the LTAG-30 device exhibited lower hysteresis, along with a lower

H-index, relative to the control device (Table S4), suggesting superior charge transfer from the PVK to the HTL in the LTAG-30 sample. Figure 3c presents the PCE distributions of the devices obtained using the LTAG and control methods. Table S5 summarizes the detailed parameters of the LTAG-30 cells. We obtained PSCs with a PCE of approximately 22% and high reproducibility, for each of the devices obtained using the LTAG method. Figure 3e displays the external quantum efficiency (EQE) spectra and the integrated values of J_{sc} of the LTAG-30 champion device. The calculated value of J_{sc} of 24.24 mA cm^{-2} matches well with the value measured (24.79 mA cm^{-2}) from the J–V curves, higher than that of the control device (Fig. S12). Figure 3f reveals a stabilized steady-state efficiency of 21.43%, with a steady-state current density of 22.24 mA cm^{-2} at a constant bias voltage of 0.96 V, for the best-performing LTAG-30 device. Figure S13 provides the corresponding data for the reference device. Furthermore, we examined the device stability at room temperature of the un-capsulated perovskite solar cells stored in a dry oven (RH = 20%; Fig. S14). The LTAG-30 device retained 90% of its initial PCE

after 1800 h; in contrast, the control device retained only 70% of its initial PCE after the same duration. Accordingly, we conclude that decreasing the amount of residual PbI$_2$ at the interface improved the device stability, possibly also by mitigating the ion migration of PbI$_2$ across the interface.

To investigate the dynamics of the photocarriers in these devices, and their relationship with the improvement in the value of V_{oc}, we recorded steady-state PL spectra of the thermally postannealed perovskite films. Figure 4a reveals that the PL intensity increased dramatically for the LTAG-30-based film relative to the control sample, implying improved photocharge properties and a decrease in the amount of spontaneous non-radiative recombination from the surface traps in the LTAG samples. We also measured the TRPL spectrum (Fig. 4b) as dots, which we fitted using a biexponential decay function (solid lines) featuring fast (τ_1) and slow (τ_2) decay times [56]. We derived average lifetime constants of 497.81 and 846.03 ns for the control and LTAG-30 films, respectively (Table S6). The LTAG-based film possessed the longer average lifetime, indicating a decrease in its non-radiative recombination and potentially passivated
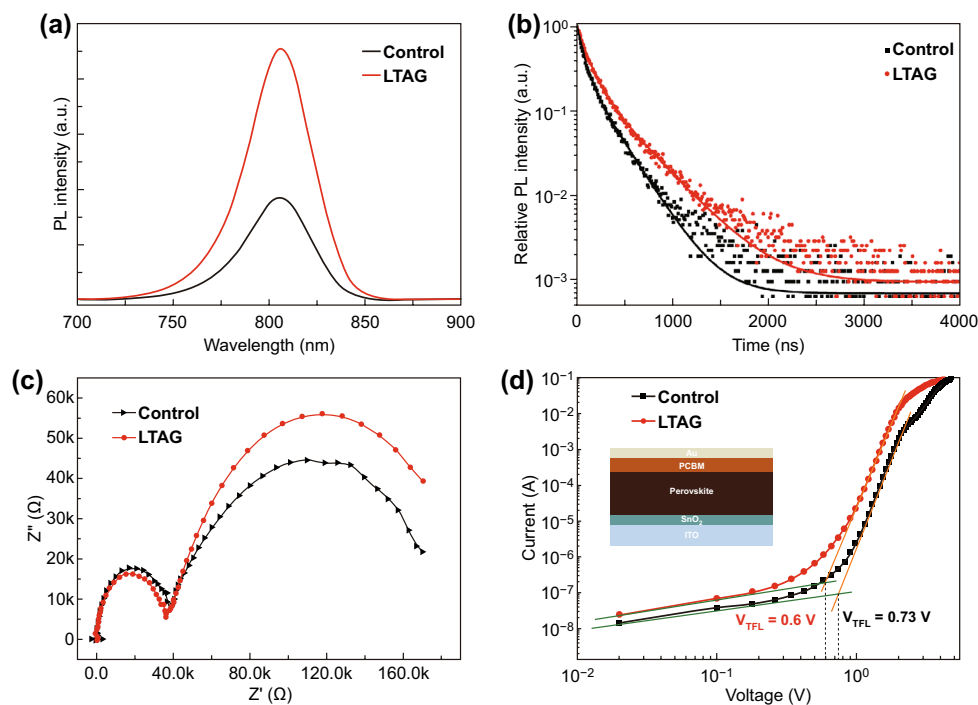
Fig. 4 a Steady-state PL spectra of annealed perovskite layers prepared without (control) and with LTAG treatment at 30 °C. **b** TRPL spectra of the control and LTAG-based perovskite films. **c** Nyquist plots for the control and LTAG-based perovskite devices in the dark. **d** Current–voltage curves and extracted defect densities of electron-only devices prepared using the control and LTAG-based methods; insets: the single-carrier device structures

surface traps, arising from the well-controlled residual PbI_2 content across the perovskite layer surface. We used EIS to study the interfacial charge transfer properties. As displayed in Fig. 4c, the high and low frequencies corresponded to the bulk transfer (R_{tr}) and interface recombination (R_{rec}) resistances in the perovskite device, respectively [57]. Compared with the control sample, we measured a lower value of R_{tr} and a higher value of R_{rec} in the LTAG sample (Fig. S15, Table S7), suggesting that charge transfer across the bulk material and the contact interface had both improved in the LTAG-based device.

We used the SCLC method to examine the decrease in the defect density for our devices, employing the following electron-only device configuration: $ITO/SnO_2/FAMAPbI_3/PC_{61}BM/Au$. Figure 4d reveals three different regions in the logarithmic I–V curves: a linear ohmic region (slope = 1), a nonlinear trap-filling region (slope > 2), and a SCLC region (slope = 2) [58]. Upon increasing the bias voltage in region 2, the trap-filled limit voltage (V_{TFL}) was reached when all of the traps were filled, and the defect density (N_t) could be calculated from Eq. 1 [58]:

$$N_{defect} = 2\varepsilon_0\varepsilon_r V_{TFL}/eL^2 \qquad (1)$$

where ε_r is the relative permittivity of perovskite material ($\varepsilon_r = 32$) [9, 59], ε_0 is the vacuum permittivity ($\varepsilon_0 = 8.85 \times 10^{-12}$ F m^{-1}), e is the electron charge, and L is the thickness of perovskite film ($L = 800$ nm) in the devices [60]. The value of V_{TFL} decreased from 0.73 to 0.60 V after performing the aging treatment; the estimated defect density of 4.97×10^{15} cm^{-3} for the LTAG-based device was lower than that for the control reference (6.05×10^{15} cm^{-3}). This finding suggests that effective self-passivation had occurred and, thus, the number of traps had decreased. This phenomenon contributed to the observed higher values of V_{oc}, which led to the higher PCEs, of the LTAG-based solar cells [61].

Energy band alignment between the perovskite and transport layers is crucial to avoiding non-radiative recombination and V_{oc} loss at the interface [62, 63]. To examine the intrinsic cause of the improvement in the value of V_{oc} after the aging growth treatment, we used UPS to examine the electronic structure of the perovskite layers. Figure S16 presents the electronic properties of the control sample featuring an excess of residual PbI_2 and of the LTAG sample featuring the fine residual PbI_2. From the cutoff region, we found that the work functions (WFs) increased from −4.0 V for the control film to −3.9 eV for the LTAG-based film. The valence

band energies (E_{VB}) of control and LTAG-based films were −5.91 and −5.86 eV, respectively. The slight increase in the value of E_{VB} upon decreasing the amount of residual PbI_2 presumably led to a better match with the reported value of Spiro-OMeTAD (−5.22 eV), resulting in enhanced hole transport from the perovskite to the HTL and minimized carrier recombination [64], both contributing partially to the improved values of V_{oc} of our LTAG-based devices.

To identify the surface defects, we applied conductive atomic force microscopy (c-AFM) in dark to detect the phase and potential differences of the perovskite films. Figure 5a, b presents AFM phase images of the control and LTAG films, respectively. For the control film, the white PbI_2 phases had aggregated and were common on the top surface. In contrast, in the LTAG film, the crystal grains of the perovskite (observed with a dark color) were common on the top surface, with the white PbI_2 phase likely present in the grain boundary areas. Figure 5c, d presents two-dimensional (2D) surface potential spatial maps of the control and LTAG films, respectively. The potential distribution in the control perovskite film is discontinuous and surrounded by the separated white areas, suggesting high surface potential barriers exist between perovskite crystals and grain boundaries due to the excess amount of PbI_2 on the perovskite surface. However, the film provided by the LTAG method shows a relatively uniform potential distribution across the perovskite surface without any remarkable dots, indicating that a minimized surface potential barrier exists between the perovskite crystals and grain boundaries. The potential barrier between the perovskite grain and grain boundary can cause a significant influence on the carrier transfer [65]. For the control film, the surface potential of the separated white areas of PbI_2 was 40 mV higher than that of the dark areas of the bulk perovskite, indicating severe charge trapping in the PbI_2 areas. For the LTAG film, the film surface potential difference between the PbI_2 and the bulk perovskite was much lower, at 15 mV, revealing that the self-passivation of PbI_2 was highly effective and that charge trapping at the grain boundaries had been alleviated. This improvement resulted from the decreased presence of PbI_2 phases on top of the perovskite phases, enhancing the carrier transporting capability [39, 66]. These results are consistent with our experimental observations from the TRPL, EIS, SCLC, and UPS analyses, which suggested that LTAG treatment improved the values of V_{oc} and, thereby, the performance of the photovoltaic devices.
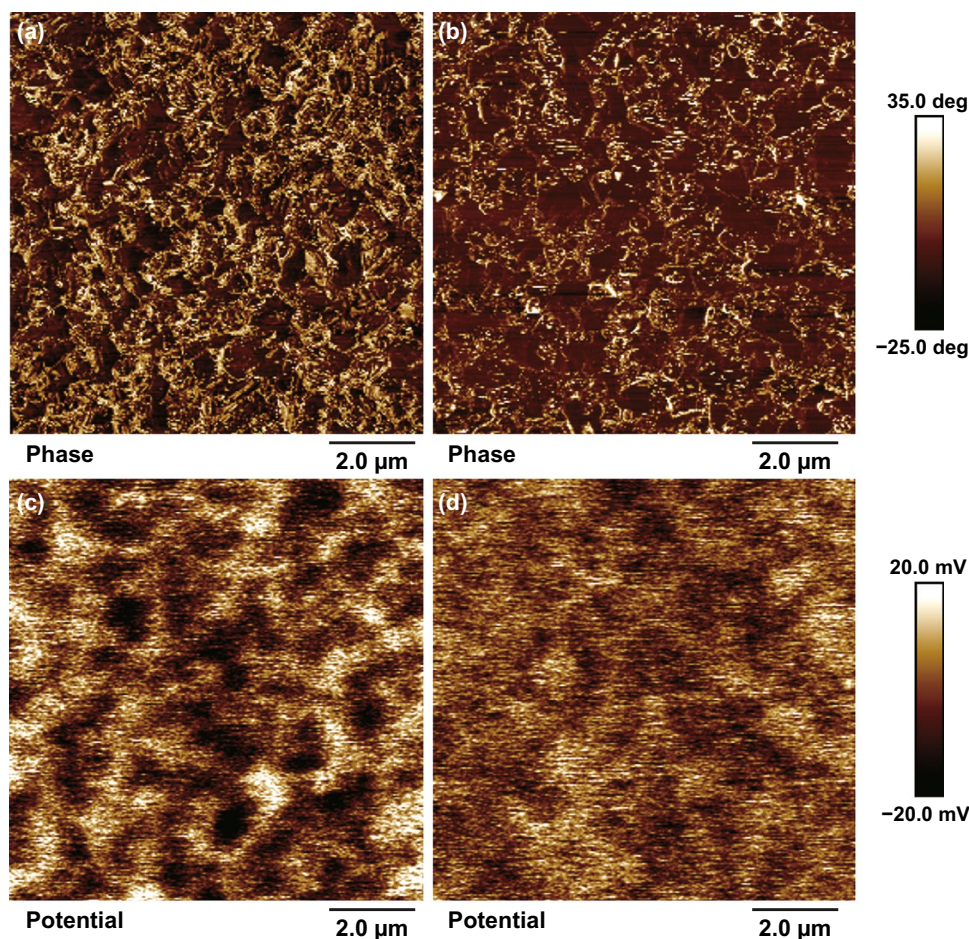
Fig. 5 **a, b** AFM phase images and **c, d** 2D surface potential spatial maps of **a, c** the control perovskite film and **b, d** the perovskite film prepared through LTAG at 30 °C

4 Conclusions

We have demonstrated that preannealing through an LTAG method produces highly crystallized and bromine-free FAMAPbI$_3$ perovskite films, with control over the content of PbI$_2$. In LTAG method, the composition of as-prepared intermediate film is optimized by inhibiting the formation of δ-phase perovskite and allowing α-phase perovskite to nucleate. Thereby, when postannealing is applied, seeded α-phase perovskites can easily turn into large grain-sized perovskites with suppressed PbI$_2$ formation. This process readily optimizes the levels of PbI$_2$ at the interface between the perovskite and the HTL and at the grain boundaries, resulting in effective self-passivation of grain boundary defects and lowering of the PVK/HTL contact resistance. Moreover, the corresponding LTAG-based devices exhibited superior PCEs of up to 22.41% with increased V_{oc} of up to 1.12 V, high reproducibility and low hysteresis. The small residual amount of PbI$_2$ created through the LTAG process was beneficial to decreasing the recombination loss on the top perovskite surface without requiring the use of an additional passivation layer or passivation agents, which may have negative effects. Therefore, this method of preannealing low-temperature aging is a simple process that provides highly efficient and reproducible low-band-gap FAMAPbI$_3$ PSCs.

References

1. A. Kojima, K. Teshima, Y. Shirai, T. Miyasaka, Organometal halide perovskites as visible-light sensitizers for photovoltaic cells. J. Am. Chem. Soc. **131**(17), 6050–6051 (2009). https://doi.org/10.1021/ja809598r

2. National Renewable Energy Laboratory, Best Research-cell Efficiency Chart. (2020). https://www.nrel.gov/pv/cell-efficiency.html. Accessed 3 Jan 2020.

3. M. Saliba, T. Matsui, K. Domanski, J.-Y. Seo, A. Ummadisingu et al., Incorporation of rubidium cations into perovskite solar cells improves photovoltaic performance. Science **354**(6309), 206–209 (2016). https://doi.org/10.1126/science.aah5557

4. M. Saliba, T. Matsui, J.Y. Seo, K. Domanski, J.P. Correa-Baena et al., Cesium-containing triple cation perovskite solar cells: improved stability, reproducibility and high efficiency. Energy Environ. Sci. **9**(6), 1989–1997 (2016). https://doi.org/10.1039/C5EE03874J

5. T. Singh, T. Miyasaka, Stabilizing the efficiency beyond 20% with a mixed cation perovskite solar cell fabricated in ambient air under controlled humidity. Adv. Energy Mater. **8**(3), 1700677 (2018). https://doi.org/10.1002/aenm.201700677

6. T. Bu, L. Wu, X. Liu, X. Yang, P. Zhou et al., Synergic interface optimization with green solvent engineering in mixed perovskite solar cells. Adv. Energy Mater. **7**(20), 1700576 (2017). https://doi.org/10.1002/aenm.201700576

7. M. Kim, G.-H. Kim, T.K. Lee, I.W. Choi, H.W. Choi et al., Methylammonium chloride induces intermediate phase stabilization for efficient perovskite solar cells. Joule **3**, 1–14 (2019). https://doi.org/10.1016/j.joule.2019.06.014

8. Y. Zhao, H. Tan, H. Yuan, Z. Yang, J.Z. Fan et al., Perovskite seeding growth of formamidinium-lead-iodide-based perovskites for efficient and stable solar cells. Nat. Commun. **9**(1), 1607 (2018). https://doi.org/10.1038/s41467-018-04029-7

9. G. Yang, H. Zhang, G. Li, G. Fang, Stabilizer-assisted growth of formamdinium-based perovskites for highly efficient and stable planar solar cells with over 22% efficiency. Nano Energy **63**, 103835 (2019). https://doi.org/10.1016/j.nanoen.2019.06.031

10. Q. Jiang, L. Zhang, H. Wang, X. Yang, J. Meng, Enhanced electron extraction using SnO_2 for high-efficiency planar-structure $HC(NH_2)_2PbI_3$-based perovskite solar cells. Nat. Energy **2**, 16177 (2016). https://doi.org/10.1038/nenergy.2016.177

11. H. Tan, A. Jain, O. Voznyy, X. Lan, F.P. García de Arquer, J.Z. Fan et al., Efficient and stable solution-processed planar perovskite solar cells via contact passivation. Science **355**(6326), 722–726 (2017). https://doi.org/10.1126/science.aai9081

12. M. Singh, A. Ng, Z. Ren, H. Hu, H.-C. Lin, C.-W. Chu, G. Li, Facile synthesis of composite tin oxide nanostructures for high-performance planar perovskite solar cells. Nano Energy **60**, 275–284 (2019). https://doi.org/10.1016/j.nanoen.2019.03.044

13. S. Bai, P. Da, C. Li, Z. Wang, Z. Yuan et al., Planar perovskite solar cells with long-term stability using ionic liquid additives. Nature **571**(7764), 245–250 (2019). https://doi.org/10.1038/s41586-019-1357-2

14. M.I. Saidaminov, J. Kim, A. Jain, R. Quintero-Bermudez, H. Tan et al., Suppression of atomic vacancies via incorporation of isovalent small ions to increase the stability of halide perovskite solar cells in ambient air. Nat. Energy **3**(8), 648–654 (2018). https://doi.org/10.1038/s41560-018-0192-2

15. D. Bi, X. Li, J.V. Milić, D.J. Kubicki, N. Pellet, J. Luo et al., Multifunctional molecular modulators for perovskite solar cells with over 20% efficiency and high operational stability. Nat. Commun. **9**(1), 4482 (2018). https://doi.org/10.1038/s41467-018-06709-w

16. L. Chao, Y. Xia, B. Li, G. Xing, Y. Chen, W. Huang, Room-temperature molten salt for facile fabrication of efficient and stable perovskite solar cells in ambient air. Chem **5**(4), 995–1006 (2019). https://doi.org/10.1016/j.chempr.2019.02.025

17. J.J. Yoo, S. Wieghold, M.C. Sponseller, M.R. Chua, S.N. Bertram et al., An interface stabilized perovskite solar cell with high stabilized efficiency and low voltage loss. Energy Environ. Sci. **12**(7), 2192–2199 (2019). https://doi.org/10.1039/C9EE00751B

18. S. Yang, J. Dai, Z. Yu, Y. Shao, Y. Zhou, X. Xiao, X.C. Zeng, J. Huang, Tailoring passivation molecular structures for extremely small open-circuit voltage loss in perovskite solar cells. J. Am. Chem. Soc. **141**(14), 5781–5787 (2019). https://doi.org/10.1021/jacs.8b13091

19. Y. Zhang, G. Grancini, Z. Fei, E. Shirzadi, X. Liu et al., Auto-passivation of crystal defects in hybrid imidazolium/methylammonium lead iodide films by fumigation with methylamine affords high efficiency perovskite solar cells. Nano Energy **58**, 105–111 (2019). https://doi.org/10.1016/j.nanoen.2019.01.027

20. S. Pang, H. Hu, J. Zhang, S. Lv, Y. Yu et al., $NH_2CH=NH_2PbI_3$: an alternative organolead iodide perovskite sensitizer for mesoscopic solar cells. Chem. Mater. **26**(3), 1485–1491 (2014). https://doi.org/10.1021/cm404006p

21. G.E. Eperon, S.D. Stranks, C. Menelaou, M.B. Johnston, L.M. Herz, H.J. Snaith, Formamidinium lead trihalide: a broadly tunable perovskite for efficient planar heterojunction solar cells. Energy Environ. Sci. **7**(3), 982–988 (2014). https://doi.org/10.1039/C3EE43822H

22. Q. Han, S.-H. Bae, P. Sun, Y.-T. Hsieh, Y. Yang et al., Single crystal formamidinium lead iodide (FAPbI$_3$): insight into the structural, optical, and electrical properties. Adv. Mater. **28**(11), 2253–2258 (2016). https://doi.org/10.1002/adma.201505002

23. S.-H. Turren-Cruz, A. Hagfeldt, M. Saliba, Methylammonium-free, high-performance, and stable perovskite solar cells on a planar architecture. Science **362**(6413), 449–453 (2018). https://doi.org/10.1126/science.aat3583

24. D. Bi, C. Yi, J. Luo, J.-D. Décoppet, F. Zhang et al., Polymer-templated nucleation and crystal growth of perovskite films for solar cells with efficiency greater than 21%. Nat. Energy **1**, 16142 (2016). https://doi.org/10.1038/nenergy.2016.142

25. X. Zheng, B. Chen, J. Dai, Y. Fang, Y. Bai et al., Defect passivation in hybrid perovskite solar cells using quaternary ammonium halide anions and cations. Nat. Energy **2**, 17102 (2017). https://doi.org/10.1038/nenergy.2017.102

26. W.S. Yang, J.H. Noh, N.J. Jeon, Y.C. Kim, S. Ryu, J. Seo, S.I. Seok, High-performance photovoltaic perovskite layers fabricated through intramolecular exchange. Science **348**(6240), 1234–1237 (2015). https://doi.org/10.1126/science.aaa9272

27. W.S. Yang, B.-W. Park, E.H. Jung, N.J. Jeon, Y.C. Kim et al., Iodide management in formamidinium-lead-halide–based perovskite layers for efficient solar cells. Science **356**(6345), 1376–1379 (2017). https://doi.org/10.1126/science.aan2301

28. J. Burschka, N. Pellet, S.-J. Moon, R. Humphry-Baker, P. Gao, M.K. Nazeeruddin, M. Grätzel, Sequential deposition as a route to high-performance perovskite-sensitized solar cells. Nature **499**, 316–319 (2013). https://doi.org/10.1038/nature12340

29. N. Ahn, D.-Y. Son, I.-H. Jang, S.M. Kang, M. Choi, N.-G. Park, Highly reproducible perovskite solar cells with average efficiency of 18.3% and best efficiency of 19.7% fabricated via lewis base adduct of lead(II) iodide. J. Am. Chem. Soc. **137**(27), 8696–8699 (2015). https://doi.org/10.1021/jacs.5b04930

30. Y. Chen, N. Li, L. Wang, L. Li, Z. Xu, H. Jiao et al., Impacts of alkaline on the defects property and crystallization kinetics in perovskite solar cells. Nat. Commun. **10**(1), 1112 (2019). https://doi.org/10.1038/s41467-019-09093-1

31. Y. Zhao, Q. Li, W. Zhou, Y. Hou, Y. Zhao et al., Double-side-passivated perovskite solar cells with ultra-low potential loss. Solar RRL **3**(2), 1800296 (2019). https://doi.org/10.1002/solr.201800296

32. D. Bi, W. Tress, M.I. Dar, P. Gao, J. Luo, C. Renevier et al., Efficient luminescent solar cells based on tailored mixed-cation perovskites. Sci. Adv. **2**(1), e1501170 (2016). https://doi.org/10.1126/sciadv.1501170

33. Q. Jiang, Z. Chu, P. Wang, X. Yang, H. Liu et al., Planar-structure perovskite solar cells with efficiency beyond 21%. Adv. Mater. **29**(46), 1703852 (2017). https://doi.org/10.1002/adma.201703852

34. Q. Jiang, Y. Zhao, X. Zhang, X. Yang, Y. Chen et al., Surface passivation of perovskite film for efficient solar cells. Nat. Photonics **13**(7), 460–466 (2019). https://doi.org/10.1038/s41566-019-0398-2

35. S. Yang, S. Chen, E. Mosconi, Y. Fang, X. Xiao et al., Stabilizing halide perovskite surfaces for solar cell operation with wide-bandgap lead oxysalts. Science **365**(6452), 473–478 (2019). https://doi.org/10.1126/science.aax3294

36. B.-W. Park, S.I. Seok et al., Intrinsic instability of inorganic–organic hybrid halide perovskite materials. Adv. Mater. **31**(20), 1805337 (2019). https://doi.org/10.1002/adma.201805337

37. G.S. Shin, S.G. Kim, Y. Zhang, N.G. Park, A correlation between iodoplumbate and photovoltaic performance of perovskite solar cells observed by precursor solution aging. Small Methods (2019). https://doi.org/10.1002/smtd.201900398

38. H. Zhou, Q. Chen, G. Li, S. Luo, T.-B. Song et al., Interface engineering of highly efficient perovskite solar cells. Science **345**(6196), 542–546 (2014). https://doi.org/10.1126/science.1254050

39. Q. Chen, H. Zhou, T.-B. Song, S. Luo, Z. Hong et al., Controllable self-induced passivation of hybrid lead iodide perovskites toward high performance solar cells. Nano Lett. **14**(7), 4158–4163 (2014). https://doi.org/10.1021/nl501838y

40. C. Roldán-Carmona, P. Gratia, I. Zimmermann, G. Grancini, P. Gao et al., High efficiency methylammonium lead triiodide perovskite solar cells: the relevance of non-stoichiometric precursors. Energy Environ. Sci. **8**(12), 3550–3556 (2015). https://doi.org/10.1039/C5EE02555A

41. Y.C. Kim, N.J. Jeon, J.H. Noh, W.S. Yang, J. Seo et al., Beneficial effects of PbI$_2$ incorporated in organo-lead halide perovskite solar cells. Adv. Energy Mater. **6**(4), 1502104 (2016). https://doi.org/10.1002/aenm.201502104

42. L. Wang, C. McCleese, A. Kovalsky, Y. Zhao, C. Burda, Femtosecond time-resolved transient absorption spectroscopy of CH$_3$NH$_3$PbI$_3$ perovskite films: evidence for passivation effect of PbI$_2$. J. Am. Chem. Soc. **136**(35), 12205–12208 (2014). https://doi.org/10.1021/ja504632z

43. S. Li, H. Ren, Y. Yan, Boosting efficiency of planar heterojunction perovskite solar cells to 21.2% by a facile two-step deposition strategy. Appl. Surface Sci. **484**, 1191–1197 (2019). https://doi.org/10.1016/j.apsusc.2019.04.129

44. T.J. Jacobsson, J.-P. Correa-Baena, E.H. Anaraki, B. Philippe, S.D. Stranks et al., Unreacted PbI$_2$ as a double-edged sword for enhancing the performance of perovskite solar cells. J. Am. Chem. Soc. **138**(32), 10331–10343 (2016). https://doi.org/10.1021/jacs.6b06320

45. F. Liu, Q. Dong, M.K. Wong, A.B. Djurišić, A. Ng et al., Is excess PbI$_2$ beneficial for perovskite solar cell performance? Adv. Energy Mater. **6**(7), 1502206 (2016). https://doi.org/10.1002/aenm.201502206

46. D.H. Cao, C.C. Stoumpos, C.D. Malliakas, M.J. Katz, O.K. Farha, J.T. Hupp, M.G. Kanatzidis, Remnant PbI$_2$, an unforeseen necessity in high-efficiency hybrid perovskite-based

solar cells? APL Mater. **2**(9), 091101 (2014). https://doi.org/10.1063/1.4895038

47. J. Schoonman, Organic–inorganic lead halide perovskite solar cell materials: a possible stability problem. Chem. Phys. Lett. **619**, 193–195 (2015). https://doi.org/10.1016/j.cplett.2014.11.063

48. D. Luo, W. Yang, Z. Wang, A. Sadhanala, Q. Hu et al., Enhanced photovoltage for inverted planar heterojunction perovskite solar cells. Science **360**(6396), 1442–1446 (2018). https://doi.org/10.1126/science.aap9282

49. K. Meng, X. Wang, Q. Xu, Z. Li, Z. Liu et al., In situ observation of crystallization dynamics and grain orientation in sequential deposition of metal halide perovskites. Adv. Funct. Mater. **29**(35), 1902319 (2019). https://doi.org/10.1002/adfm.201902319

50. L. Wang, X. Wang, L.-L. Deng, S. Leng, X. Guo et al., The mechanism of universal green antisolvents for intermediate phase controlled high-efficiency formamidinium-based perovskite solar cells. Mater. Horizons (2020). https://doi.org/10.1039/C9MH01679A

51. P. Zhao, B.J. Kim, X. Ren, D.G. Lee, G.J. Bang et al., Antisolvent with an ultrawide processing window for the one-step fabrication of efficient and large-area perovskite solar cells. Adv. Mater. **30**(49), 1802763 (2018). https://doi.org/10.1002/adma.201802763

52. S. Paek, P. Schouwink, E.N. Athanasopoulou, K.T. Cho, G. Grancini et al., From nano- to micrometer scale: the role of antisolvent treatment on high performance perovskite solar cells. Chem. Mater. **29**(8), 3490–3498 (2017). https://doi.org/10.1021/acs.chemmater.6b05353

53. N.J. Jeon, J.H. Noh, Y.C. Kim, W.S. Yang, S. Ryu, S.I. Seok, Solvent engineering for high-performance inorganic–organic hybrid perovskite solar cells. Nat. Mater. **13**(9), 897–903 (2014). https://doi.org/10.1038/nmat4014

54. Y. Chen, Q. Meng, Y. Xiao, X. Zhang, J. Sun et al., Mechanism of PbI$_2$ in situ passivated perovskite films for enhancing the performance of perovskite solar cells. ACS Appl. Mater. Interfaces. **11**(47), 44101–44108 (2019). https://doi.org/10.1021/acsami.9b13648

55. A. Alberti, I. Deretzis, G. Mannino, E. Smecca, F. Giannazzo et al., Nitrogen soaking promotes lattice recovery in polycrystalline hybrid perovskites. Adv. Energy Mater. **9**(12), 1803450 (2019). https://doi.org/10.1002/aenm.201803450

56. W.F. Wei, B. Jiao, H. Dong, J. Xu, T. Lei et al., Bifunctional π-conjugated ligand assisted stable and efficient perovskite solar cell fabrication via interfacial stitching. J. Mater. Chem. A **7**(27), 16533–16540 (2019). https://doi.org/10.1039/C9TA03898A

57. D. Yang, R. Yang, K. Wang, C. Wu, X. Zhu et al., High efficiency planar-type perovskite solar cells with negligible hysteresis using EDTA-complexed SnO$_2$. Nat. Commun. **9**(1), 3239 (2018). https://doi.org/10.1038/s41467-018-05760-x

58. S. Wang, Y. Zhu, C. Wang, R. Ma, Interface modification by a multifunctional ammonium salt for high performance and stable planar perovskite solar cells. J. Mater. Chem. A **7**(19), 11867–11876 (2019). https://doi.org/10.1039/C9TA02631B

59. Q. Dong, Y. Fang, Y. Shao, P. Mulligan, J. Qiu, L. Cao, J. Huang, Electron-hole diffusion lengths > 175 μm in solution-grown CH$_3$NH$_3$PbI$_3$ single crystals. Science **347**(6225), 967–970 (2015). https://doi.org/10.1126/science.aaa5760

60. T. Chen, G. Tong, E. Xu, H. Li, P. Li et al., Accelerating hole extraction by inserting 2D Ti$_3$C$_2$-mxene interlayer to all inorganic perovskite solar cells with long-term stability. J. Mater. Chem. A **7**(36), 20597–20603 (2019). https://doi.org/10.1039/C9TA06035A

61. Z. Liu, L. Qiu, E.J. Juarez-Perez, Z. Hawash, T. Kim et al., Gas-solid reaction based over one-micrometer thick stable perovskite films for efficient solar cells and modules. Nat. Commun. **9**(1), 3880 (2018). https://doi.org/10.1038/s41467-018-06317-8

62. M. Stolterfoht, P. Caprioglio, C.M. Wolff, J.A. Márquez, J. Nordmann et al., The impact of energy alignment and interfacial recombination on the internal and external open-circuit voltage of perovskite solar cells. Energy Environ. Sci. **12**(9), 2778–2788 (2019). https://doi.org/10.1039/C9EE02020A

63. H. Hu, S. Birkhold, M. Sultan, A. Fakharuddin, S. Koch, L. Schmidt-Mende, Surface band bending influences the open-circuit voltage of perovskite solar cells. ACS Appl. Energy Mater. **2**(6), 4045–4052 (2019). https://doi.org/10.1021/acsaem.9b00060

64. N. Li, S. Tao, Y. Chen, X. Niu, C.K. Onwudinanti, C. Hu et al., Cation and anion immobilization through chemical bonding enhancement with fluorides for stable halide perovskite solar cells. Nat. Energy **4**(5), 408–415 (2019). https://doi.org/10.1038/s41560-019-0382-6

65. G. Tong, T. Chen, H. Li, L. Qiu, Z. Liu et al., Phase transition induced recrystallization and low surface potential barrier leading to 10.91%-efficient CsPbBr 3 perovskite solar cells. Nano Energy **65**, 104015 (2019). https://doi.org/10.1016/j.nanoen.2019.104015

66. J.-H. Lee, J. Kim, G. Kim, D. Shin, S.Y. Jeong et al., Introducing paired electric dipole layers for efficient and reproducible perovskite solar cells. Energy Environ. Sci. **11**(7), 1742–1751 (2018). https://doi.org/10.1039/C8EE00162F